22 Impact of turbulence on cloud microphysics

Gholamhossein Bagheri[1], Eberhard Bodenschatz[1], John Lawson[2], Jan Moláček[1], Freja Nordsiek[1], Oliver Schlenczek[1]

22.1 Introduction

Clouds consist of water droplets and ice particles that are dispersed within a highly non-stationary, inhomogeneous, and intermittent turbulent flow (Bodenschatz et al. 2010). Earth's atmosphere is dominated by the presence of clouds, which exert great control on the Earth's radiative balance, which strongly impacts weather and climate. Despite decades of research, a vast community of scientists and considerable measurement infrastructure (e.g. weather stations and satellites), insufficient understanding of cloud physics (moist convection and cloud evolution) is a primary source of uncertainty in weather and climate models (Stevens & Bony 2013). Why can't we reliably predict weather more than a few days ahead (and sometimes not even a few hours), let alone forecast the climate in 50 years?

Various factors can be blamed for the 'cloud challenge'. Two key factors are the enormous scale separations in cloud physics and turbulence (Bodenschatz et al. 2010). Physical phenomena related to formation and evolution of clouds span a wide range of scales from micrometres (scale of small cloud particles and aerosols) to hundreds of kilometres where clouds become part of global weather and climate. Additionally, there is a strong interplay and coupling with turbulence at all scales. In particular, the challenge is to incorporate the microphysical processes occurring at sub-metre scales, such as inertial clustering and entrainment of environmental air in clouds, into coarse-resolution weather and climate models. Even before that, we are yet to understand how such microphysical processes work (Stevens & Bony 2013; Bodenschatz 2015; Beals et al. 2015).

22.1.1 Rain initiation problem

"According to the Mt. Washington experiments, we should expect that droplets in summer cumulus clouds at +20C should grow to a diameter of about 26 microns in one minute and to about 72 microns in thirty minutes. … Since cumulus clouds often develop rain within less than thirty minutes after their formation, we see that some mechanism other than that assumed in the evaporation-condensation theory must be involved in rain formation." Irving Langmuir (1948)

Seventy years after Langmuir's statement, we still don't understand the rapid growth of 30–80 µm diameter (d_p) drops in warm (ice-free) clouds (the growth of ice particles in mixed-phase clouds has been explained by the Wegener-Bergeron-Findeisen process since 1938, see Wallace & Hobbs, 2006). It is well understood that nucleation-condensation explains the rapid growth of d_p from sub-micron formation to 30 µm. At the same time, gravitational collisions explain the growth of drops with $d_p > 80$ µm (section 7 in Pumir & Wilkinson, 2016). However, for 30–80 µm drops the growth process is still poorly understood (Grabowski & Wang 2013; Pumir & Wilkinson 2016). It is believed that these drops also grow by collision-coalescence, but the underlying mechanisms, and in particular the role of turbulence, need to be explained. In the following discussion, we will limit ourselves to the case of warm clouds – those consisting entirely of liquid water droplets, and thus talk only about rain.

22.1.2 The nature of turbulence in clouds

"The essential point is that fluid motion is almost always inherently unstable, and that incipient instabilities are suppressed only if the viscous dissipation is high enough. However, virtually all fluids have an extremely low viscosity. This is true of water, air, blood, the molten metal in the core of the earth, and the atmosphere of the sun. The implication is that turbulence is the natural state of things and indeed this is the case." Davidson (2015)

[1] Max Planck Institute for Dynamics and Self-Organization, Am Faßberg 17, 37077 Göttingen, Germany
[2] Aerodynamics and Flight Mechanics Research Group, University of Southampton, Southampton SO17 1BJ, UK

22

Atmospheric turbulence is characterized by its large separation of scales. One measure of this is the large-eddy Reynolds number:

$$Re_\ell = u'l/v \tag{1}$$

where u' is the fluctuating (root-mean-square) turbulent velocity, l is the integral length scale (i.e. the length scale of the flux carrying eddies $\sim 10^2$–10^3 m) and v is the kinematic viscosity ($\sim 10^{-5}$ m^{2}s^{-1} for air). u' in clouds can vary over at least two orders of magnitude with a typical moderate cumulus cloud value of 1 m s^{-1} (Shaw 2003). Since most turbulent kinetic energy is in the large eddies, we can safely replace u' by the fluctuating velocity of large eddies, i.e. $Re_\ell = u_\ell l/v$. For atmospheric clouds, Re_ℓ is typically $\sim 10^6$–10^8.

According to Richardson's (1922) energy-cascade theory, the kinetic energy of velocity fluctuations in fully-developed turbulence cascades from large energy-containing scales (l) to smaller scales until it dissipates to heat. Dimensional analysis shows turbulence energy production scales as u_ℓ^3/l. Since a fully-developed turbulent flow cascade is a stationary state, the rate at which kinetic energy is transferred to the smaller scales is equal to the rate it is viscously dissipated ε:

$$\varepsilon \sim u_\ell^3/l, \tag{2}$$

which is one of the most important turbulence parameters. As an example in the spirit of the Kolmogorov (1941) hypotheses, knowing ε allows the estimate of various temporal and spatial scales of turbulence, scaling of the turbulence energy spectrum in intermediate length scales (inertial range), and statistics of low-order velocity increments. The cloud-average ε for moderate cumulus clouds is typically around 10^{-2} m^{2}s^{-3}. However, ε inside clouds can vary by several orders of magnitude with the highest values occurring typically around the cloud top (~ 0.1 m^{2}s^{-3}) and smaller values at the cloud base around $\sim 10^{-3}$ – 4×10^{-3} m^{2}s^{-3} (Vaillancourt & Yau 2000; Shaw 2003).

The dissipation scales are called the Kolmogorov microscales of turbulence (Davidson 2015). The Kolmogorov length scale η is derived through dimensional analyses based on Kolmogorov's first similarity hypothesis (small-scale statistics in fully-developed turbulence should only depend on v and ε)

$$\eta = \left(v^3/\varepsilon\right)^{1/4}. \tag{3}$$

Similarly, we can define Kolmogorov time τ_η and velocity u_η scales

$$\tau_\eta = (v/\varepsilon)^{1/2}, \tag{4}$$

$$u_\eta = (v\varepsilon)^{1/4}. \tag{5}$$

The Kolmogorov scale Reynolds number, $Re_\eta = \eta u_\eta/v$, is of order unity, which is consistent with the energy-cascade picture that viscous dissipation dominates at Kolmogorov scales. For atmospheric clouds, η – 1 mm, $\tau_\eta \sim 10$ ms, and $u_\eta \sim 1$ cm s^{-1}. Combining equations (1) to (5), one can see that the cloud scale separation l/η scales with $Re_l^{3/4}$. Considering that $Re_l \sim 10^6$–10^8 in clouds, the scale separation is $O(10^4)$ – $O(10^6)$.

The Taylor microscale Reynolds number, $Re_\lambda = u_l\lambda/v \sim (15\,Re_l)^{1/2}$, is often used for quantifying turbulence strength. The Taylor length microscale, $\lambda \sim \left(u_l^2 v/\varepsilon\right)^{1/2}$, is the characteristic length scale of the mean spatial extension of velocity gradients, which lies between l and η (Vaillancourt & Yau 2000). Unlike Re_l (which depends on the non-universal, flow-dependent, scales of large eddies) and Re_η (always of order unity), Re_λ is an appropriate dimensionless number for comparing universal statistics of different turbulent flows with each other since it is based on an intermediate length scale with universal characteristics. In clouds, $Re_\lambda \sim 10^4$.

The dispersion and interaction of cloud particles with turbulence is of great interest. The 30–80 µm drops at the heart of the cloud problem are much smaller than η in typical clouds. Experimental measurements, such as the pioneering investigation of Snyder & Lumley (1971), have shown that the main parameters controlling dispersion of particles $d_p \ll \eta$ in a turbulent flow are the particle-to-fluid density ratio and Stokes number

$$St = \frac{\tau_p}{\tau_\eta} = \frac{\rho_p \varepsilon^{1/2} d_p^2}{18\rho_f v^{3/2}}, \tag{6}$$

where $\tau_p = \rho_p d_p^2/18\rho_f \nu$ and ρ_p are the particle relaxation (or response) time and density, and ρ_f is the fluid density. St is a measure of particle inertia – $St \ll 1$ particles follow the fluid flow faithfully, while $St \gg 1$ particles are completely decoupled from the flow. Typical values of St for 10–100 µm cloud drops are 10^{-2}–10^0. Table 1 summarizes typical turbulence-cloud parameters.

Tab. 1: Ranges and values of important cloud-turbulence parameters typically encountered in free cumulus clouds and at the UFS.

Parameter	Typical range	Typical value	Meas. at UFS
ε [m²s⁻³]	10^{-3}–10^{-1}	1×10^{-2}	8×10^{-2}
η [m]	10^{-4}–10^{-3}	8×10^{-4}	4×10^{-4}
τ_η [s]	10^{-2}–10^{-1}	4×10^{-2}	1×10^{-2}
u_η [ms⁻¹]	10^{-2}–10^{-1}	2×10^{-2}	3×10^{-2}
Re_λ	10^3–10^4	8×10^3	3×10^3
St	10^{-3}–10^0*	3×10^{-1}*	5×10^{-2}**

* considering cloud drops with diameters of 10–50 µm and mean of 30 µm.

** see Fig. 9 and 10 in Siebert et al. (2015).

22.1.3 Characteristics of clouds at the UFS

Measurements indicate that the microphysical and turbulent properties of clouds at the UFS are representative of free clouds, which makes the UFS a suitable site for investigating clouds. Easterly-westerly winds are dominant at the UFS as a result of the local topography (Fig. 1a). Warm clouds are dominant in the average 5°C summer. Wind speeds with and without clouds were usually < 14 ms⁻¹ with a most probable value of ~0.9 ms⁻¹ and an average of 1.2–2.6 ms⁻¹ for 2000–2012 (Risius et al. 2015; Siebert et al. 2015), which can be seen in Figure 1b. The velocity energy spectrum measured by an ultrasonic anemometer and a hotwire at the UFS and the weather data from the DWD (Deutscher Wetterdienst) from the peak of the Zugspitze are shown together in Figure 1c (Risius et al. 2015).

Ultrasonic anemometry at the UFS indicates the RMS velocity is $u' \approx 1$ ms⁻¹ (Risius 2012). Taking the approximate distance from the measurement point to the mountainside to be the large eddy scale of $l \sim 10$ m, we obtain $\varepsilon \sim u'^3/l \approx 10^{-1}$ m²s⁻³, which is comparable to $\varepsilon = 8.5 \times 10^{-2}$ m²s⁻³ meas-
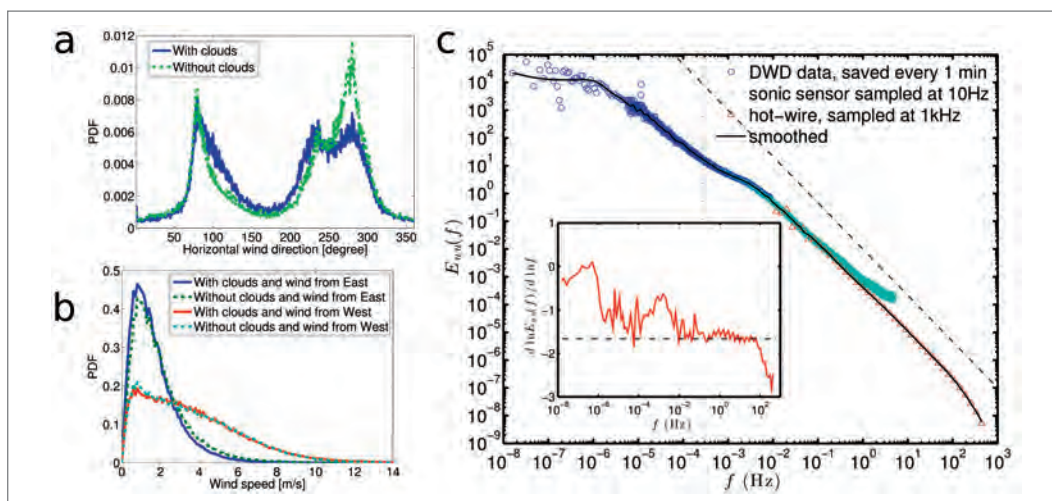

Fig. 1: Wind data from the Zugspitze (Risius et al. 2015). (a) Wind direction angle PDF and (b) speed PDF for the most common directions at the UFS measured by an ultrasonic anemometer (Fig. 4) in cloudy and non-cloudy conditions. (c) Turbulent energy spectrum of east-west wind on the Zugspitze. Hotwire and sonic data are from the UFS, and the DWD data is from the peak. The solid black line is the smoothed composite spectrum. The diagonal dash-dotted line is a Kolmogorov $f^{-5/3}$ spectrum line, and the vertical dashed line corresponds to 1 hr^{-1}. The inset shows the composite spectrum's local logarithmic slope compared to the Kolmogorov –5/3 spectrum (horizontal line).

ured by hot-wire anemometry (Siebert et al. 2015). $Re_l \sim 10^6$, which is at the low end for free clouds in the atmospheric boundary layer (Siebert, Lehmann, Wendisch, et al. 2006). The maximum Re_λ is of the order of 10^4 with a most common value of ~3000 (Risius et al. 2015). These values are summarized in Table 1.

22.1.4 Physics of Rain Initiation

Every raindrop starts as a cloud condensation nucleus, a sub-micron aerosol particle (salt crystals, organic molecules, combustion residue, etc.) suspended in air. As the excess relative humidity greater than 100 % (supersaturation) rises above a critical level, water vapor quickly condenses on the nucleus which acts as a catalyst. The droplet's radius grows over time proportionally to the local supersaturation level, which can be caused by adiabatic cooling such as what happens when an airmass flows up a mountain. At the same time, $dr/dt \sim r^{-1}$. Thus a period of rapid growth is followed by progressive slowdown, resulting in an increasingly narrow droplet size distribution where younger drops catch up with older ones.

Initially, the droplets have a settling speed much smaller than the typical updraft speeds effectively suspending them in the flow (a 20 μm diameter droplet has a settling speed of 2 cm/s whereas updrafts are typically several m/s). To reach sufficiently high settling speeds to overcome the updraft and fall to the ground, the droplets have to reach diameters of several hundred μm. Raindrop sizes typically follow an exponential distribution (Jameson & Kostinski 2001; Marshall & Palmer 1948) with the mean drop size increasing with increasing rain rate, and can reach up to and beyond the maximum stable diameter of about 6 mm (Gunn & Kinzer 1949).

For a droplet to reach millimetric raindrop size purely by condensational growth would take orders of magnitude longer than what is observed. This leaves only combining droplets together by various collision-coalescence processes. The simplest model for the evolution of droplet size distribution by collisions is

$$\frac{\partial n(r,t)}{\partial t} = \frac{1}{2} \int_0^r K(s, r') \left| \frac{\partial r'}{\partial r} \right|^{-1} n(s, t) \, n(r', t) \, ds - n(r, t) \int_0^\infty K(r, s) \, n(s, t) \, ds, \qquad (7)$$

where $n(r, t)$ is the number density of droplets of radius r at time t, $K(s, r)$ is the coalescence kernel giving the rate of coalescence between drops of radius s and r, and $r' = (r^3 - s^3)^{1/3}$ is the required drop radius to form a drop of radius r *when coalescing with a drop of radius s.* The first integral is the rate of increase of $n(r, t)$ due to coalescence of smaller droplets, whereas the second term describes the decrease of $n(r, t)$ due to coalescence of droplets with radius r with other droplets.

In this simplest model, coalescence is assumed to happen whenever two droplets collide. In reality, this is only approximately true for large drops with small relative velocities. Large drops with large relative velocities tend to produce several droplets, and small droplets often move around each other due the hydrodynamics of the gas between them. Henceforth we shall replace the coalescence kernel with the collision kernel. For drops moving in still air solely due to gravity where the typical time between collisions is larger than the relaxation time for droplets to reach terminal velocity, the collision kernel is simply

$$K_G(r, s) = \pi (r + s)^2 |V(r) - V(s)|, \qquad (8)$$

where $V(r)$ is the settling speed of a drop with radius r, and $\pi (r + s)^2$ is the combined collision cross-section area.

While a modified version of (7)–(8) that accounts for the collision and coalescence efficiency describes the latest stages of large drop growth well, its fundamental weakness is that it depends on the differential settling speed, and hence differential size, to drive the collisions; so that it cannot explain how the initially narrow size distribution of small droplets produced by condensational can grow and broaden within a reasonable timeframe. This is where turbulence comes in. By creating shear down to η, turbulent flow makes it possible for even equally sized droplets to collide. Careful analysis (Saffman & Turner 1956) yields a turbulent shear collision kernel

$$K_{TS}(r, s) = 1.3 (r + s)^3 \tau_\eta. \qquad (9)$$

Unequally sized droplets respond differently to turbulent acceleration due to their different inertias, which enhances collision probability. The process' collision kernel is (Levich 1954)

$$K_{TI}(r, s) = \pi(r + s)^2 |\tau_p(r) - \tau_p(s)| a_\eta, \tag{10}$$

where $a_\eta = \eta/\tau_\eta^2$ is the Kolmogorov acceleration. Even with these effects taken into account, the droplet growth rate at 20–100 μm diameter is still significantly underestimated.

These collision kernels have all been obtained under the assumption that the spatial distribution of droplets is uniformly random – that is, the likelihood of finding a given droplet at any location is the same. However, numerical simulations of particles in turbulent flows have shown that the particles actually cluster onto lower-dimensional fractal-like structures (Yoshimoto & Goto 2007). The level of clustering is dependent on the particle inertia. Particles with little inertia behave like passive tracers, faithfully following the surrounding flow, which, by virtue of its incompressibility do not cluster. Conversely, particles with large inertia cannot respond to the quick changes in the local flow conditions, effectively averaging flow structure over larger scales, which tends to lead to much weaker net effect on their trajectories. Thus, the uniform spatial distribution assumption holds for very small (d_p < 10 μm) and large (d_p > 100 μm); while for intermediate drop sizes, where the drop response time is comparable to τ_η, the clustering can produce structures with fractal dimension as low as 2.3 (Bec et al. 2007). The lower the fractal dimension, the more likely it is to find two drops very close to each other, which increases the collision rate.

The collision rate is also enhanced by caustics in the droplet velocity field due to the so-called sling effect (Falkovich et al. 2002) where the droplet velocity field becomes multivalued as droplet trajectories separating from regions of different air velocity cross. This allows droplets with significantly different velocities to come close to each other, which enhances not only their collision rate but also the collision efficiency. While the acceleration magnitudes required to create the sling effect for droplet size of interest are substantially higher than the typical accelerations encountered in the flow, turbulence is known to create these extreme events with a likelihood far larger than would be expected from a normal distribution (La Porta et al. 2001).

The approaches described up to now all start from some version of equation (7). This equation describes the droplet number density as if it were a continuous quantity evolving deterministically. In a real cloud, the droplet numbers are discrete and their collisions are a stochastic process – if we were to start from macroscopically identical initial conditions, the sequence of collisions would be different for each repetition. Since it takes about one million 10 μm diameter drops to produce a typical raindrop, one in a million droplets coalescing could be enough for a runaway process of growth by coalescence to start. Therefore, a relatively small number of discrete collision events can have a large impact on the total timescale of the rain initiation, which can lead to an underestimate of the droplet growth rate using the continuous model Eq. (7) compared to a stochastic approach (Kostinski & Shaw 2005). Furthermore, it highlights the need to understand the nature and likelihood of the rare events in which the first millionth of droplets collide. Such understanding necessitates collecting large amounts of data resolving the smallest spatial and time-scales at which these events occur.

22.1.5 Available methods

Turbulence-cloud interactions are analysed at various scales with theoretical analyses, numerical simulations, and laboratory and in-situ (field) measurements. Solving the Navier-Stokes equations (the equations of motion for fluids like air) by Direct Numerical Simulation (DNS) or Large Eddy Simulation (LES) are the two main computational approaches. With LES, the small scales are modelled indirectly while large scales are computed directly, which allows high Re_λ to be reasonably well simulated (Warhaft 2002) at the expense of fine-scale turbulent features (mixing, fluctuations, etc.) and particle-turbulent interaction. DNS, on the other hand, simulates all scales, but the computational cost increases rapidly as Re_λ and, therefore, l/η grows. Specifically, projecting the costs from $Re_\lambda \sim 10^3$ to 10^4, yields 20–100 weeks on the fastest supercomputer available today[3] for one eddy turnover time depending on the computational efficiency of the code (e. g. see Jimenez, 2003, for computational requirments), and that is without taking

---

[3] https://www.top500.org/, November 2017 list

temperature, buoyancy, vapor, and particles into account. It will take years (if ever) before turbulent flows similar to clouds can be simulated. Nevertheless, DNS can provide detailed information on statistics of small-scale fluctuations in velocity, temperature, and water-vapour mixing ratio and droplet collision-coalescence (Balachandar & Eaton 2010; Grabowski & Wang 2013; Pumir & Wilkinson 2016).

Innovative experimental measurements are required to bridge the scales and develop validated sub-grid models for simulations and models.

Currently, creating real cloud conditions in laboratory experiments is very difficult. The difficulty is ro reach cloud Re_λ with small cloud ε while ensuring that the gravitational settling is not negligible. Laboratory flows with low ε must either be very large or have Re_λ smaller than clouds. However, recently-developed turbulence wind tunnels, such as those developed by Bodenschatz et al. (2014), can produce decaying isotropic turbulence with $Re_\lambda \sim 6000$ and $\varepsilon \sim 0.1$ m^{2}s^{-3}, which is promising.

Field observations in actual clouds are one of the most promising options. Most field observations are carried out with airborne campaigns that are flexible in picking clouds of interest away from ground topographical effects (Siebert, Lehmann, Wendisch, et al. 2006; Siebert et al. 2010; Malinowski et al. 2013; Beals et al. 2015). Aircraft-based measurements, however, are constrained by the resolution of flight speed and sampling frequency. A solution is to use blimps, aerostats, or kites; which are constrained by the wind speed instead of flight speed (Siebert, Lehmann & Wendisch 2006). Typical wind speeds encountered by aerostats are ~1–10 m/s, which are an order of magnitude less than typical aircraft flight speed of ~100 m/s. Another suitable field strategy is ground-based measurements, which are not constrained by the sampling time and provide the possibility to perform Lagrangian measurements, where droplets can be tracked in time. However, there is no freedom in selecting the cloud type and topographical effects must be considered.

22.2 Measuring flow and fluid properties

A very common method of measuring temperature is thermistors – resistors whose resistance has a significant temperature dependence. Resistance Temperature Detectors (RTD) are the most popular due to their linear resistance-temperature relationship. The measurement principles are largely independent of the kind of thermistor. The resistance is measured using a small current or voltage and measuring the other, while insuring that Ohmic heating of the thermistor is negligible. A thermistor is commonly mounted inside a metal body as shown in Figure 2a and 2b or used in the so-called cold-wire configuration (shown in Figure 2c and 2d) where a thin metal wire acting as the thermistor is held between two prongs and is immersed directly in the fluid. A good example is the T-NSTAP (Temperature – Nano Scale Thermal Anemometry Probe), which has a wire thickness of 100 nm × 2 µm and a length of 200 µm allowing it to measure temperature at very fine scales (Fan et al. 2015).
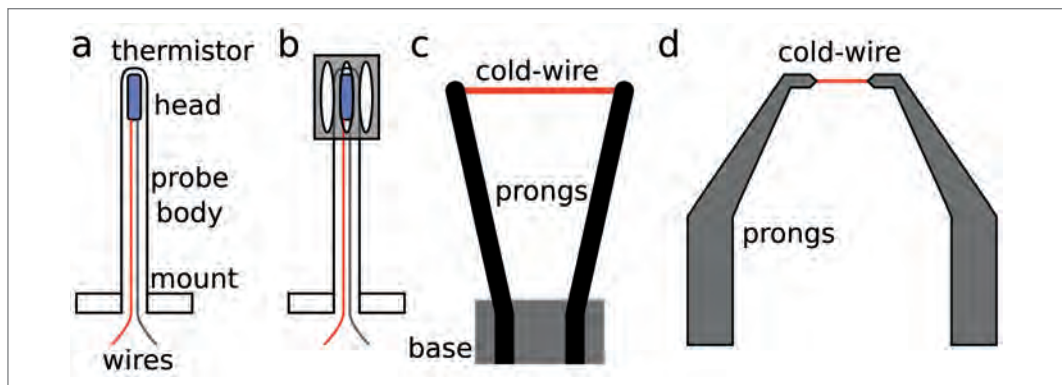

Fig. 2: (a) and (b) Diagram of two examples of thermistor probes with different housing styles. (c) and (d) Diagram of cold-wire thermistor probes, (c) being the larger conventional style and (d) being the smaller etched T-NSTAP style (Fan et al. 2015).

When Ohmic heating is not negligible, the thermistor will be significantly warmer than the surrounding fluid and exchange heat to the fluid. This is done deliberately to measure the fluid velocity. Such thermistors are known as hotwires and the technique as Hotwire Anemometry (HWA). The thermistor, almost always an RTD, is maintained at a temperature T which is greater than the fluid temperature T_f. Heat is conducted to the fluid which then diffuses and is advected away as shown in Figure 3. The heat loss P to the fluid can be approximately described by King's Law (King 1914) which is $P = (T - T_f)(A + B|u|^n)$ where n was originally derived to be ½ (King 1914) but in practice typically deviates by a small amount, u is the fluid velocity, and A and B are coefficients that depend on the wire and fluid properties. Hotwire measurements are typically done by holding the hotwire at a fixed temperature/resistance much greater than the variation in T_f with a feedback circuit, known as Constant Temperature Anemometry (CTA). The electric potential V across the hotwire is measured. Then the heat loss is just $P = V^2/R$ and the fluid velocity then easily calculated.
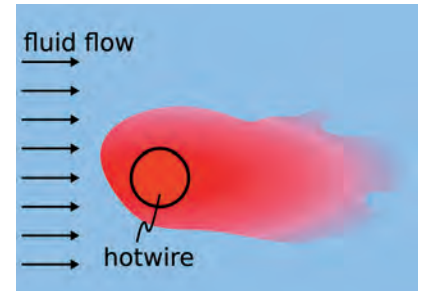

Fig. 3: Hotwire in a flowing colder fluid. The wire (seen edge on) heats the fluid which is diffused and advected away by the fluid. Elevated temperatures are shown in red.

Hotwire probes are typically used where there is a strong mean flow to measure the variation in u along the axis of the mean flow. By using the Taylor Frozen Field Hypothesis (Taylor 1938), the temporal measurements $u(t)$ can be translated to the spatial variation $u(x)$ along the mean flow direction ($U_{mean}\Delta t \approx \Delta x$). The kinetic energy spectrum can then be calculated, which allows the different scales of the fluid flow to be analysed and ε determined. Hotwires have been used to investigate the turbulent structures as well as turbulent intermittency (spatial variations in ε at small scales) in clouds (e. g. see H. Siebert et al. 2010).

Ultrasonic anemometers (sometimes called "sonics" or "sonic anemometers") are another velocity measuring device, often found in weather stations. The sonics we have on the top deck of the UFS are shown in Fig. 4 along with some wind data from Risius et al. (2015) previously in Fig. 1. The sonics consist of two or more ultrasonic transducers, which gives the advantage of having no moving parts. For a pair of transducers that can hear each other, each alternately emits a short pulse whose time of flight, Δt_{12} and Δt_{21}, to the other transducer is measured. Because sound moves relative to its medium, the travel time will be reduced or increased depending on the fluid velocity component u along the axis between the two transducers. Δt_{12} and Δt_{21} can be used to eliminate the speed of sound and the other velocity components to get $u = \frac{1}{2}L(1/\Delta t_{12} - 1/\Delta t_{21})$, where L is the distance between them (McKeon et al. 2007). Typically, several transducers are used to form enough pairs so that two or three velocity components can be resolved, and to provide redundancy when the velocity is aligned with the axis between a transducer pair (transducers disrupt the measurement). Analysis can be done using Taylor's Frozen Field Hypothesis similar to hotwires, though sonics resolve only lower frequencies.

Another quantity of interest is the water vapor concentration of the air. To measure relative humidity, three main physical mechanisms can be used: (1) change in volume or length of a hygroscopic material (the principle used in hair hygrometers), (2) change in electrical properties due to absorption of water vapor on a surface (change in capacitance, used in capacitive hy-
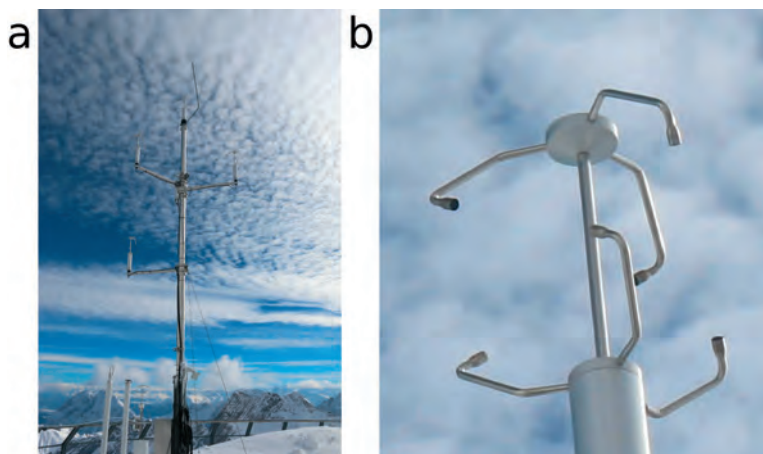

Fig. 4: (a) Picture of 6 ultrasonic anemometers, each with 6 transducers, at the UFS – 5 are on the mast and one is on the rail. (b) Picture of the rightmost ultrasonic anemometer on the mast, which has 6 transducers in an arrangement of 3 pairs.

grometers, and change in conductivity, used in lithium chloride hygrometers), and (3) spectroscopic methods (Lyman-alpha hygrometers, water vapor sensors in the near infrared) (see Harrison, 2014, for more details).

22.3 Particle Imaging Techniques

In this section, we summarise the operating principles and practical application of Particle Image Velocimetry (PIV) and Lagrangian Particle Tracking (LPT) techniques at UFS.

22.3.1 Particle Image Velocimetry

Thirty-five years since the first mention of its development in the literature, PIV capabilities have evolved from simple two-dimensional, two-component velocimetry to fully time-resolved, three-dimensional, three-component velocity, acceleration and pressure measurements (Scarano 2013). The ability to provide spatially detailed flow-field information, in comparison to single-point measurements like HWA, is perhaps why PIV has become the dominant approach to velocity measurement in experimental fluid mechanics (Westerweel et al. 2013). Several reviews and books have been dedicated to its principles and practice; in particular, Raffel (2007) and Adrian & Westerweel (2011) have become popular references amongst the fluid mechanics community.

The CloudKite PIV system, illustrated in Figure 5, has been developed to make measurements of the turbulence in clouds at UFS. The main advantages of PIV in this context are its ability to operate under variable imaging conditions and still provide comprehensive, spatial information about the turbulent flow. This allows fundamental turbulence quantities to be measured inside a cloud (turbulence intensity, structure functions, energy dissipation rate) without approximation. The basic setup is typical of 2D PIV. A dual-cavity laser is equipped with cylindrical lenses to generate a "light sheet", which provides pulsed, planar illumination of seeding particles (droplets) embedded in the flow. A digital camera records pairs of images illuminated by sequential light pulses, separated by a time interval Δt. The velocity field is inferred from the displacement of particles over this interval.
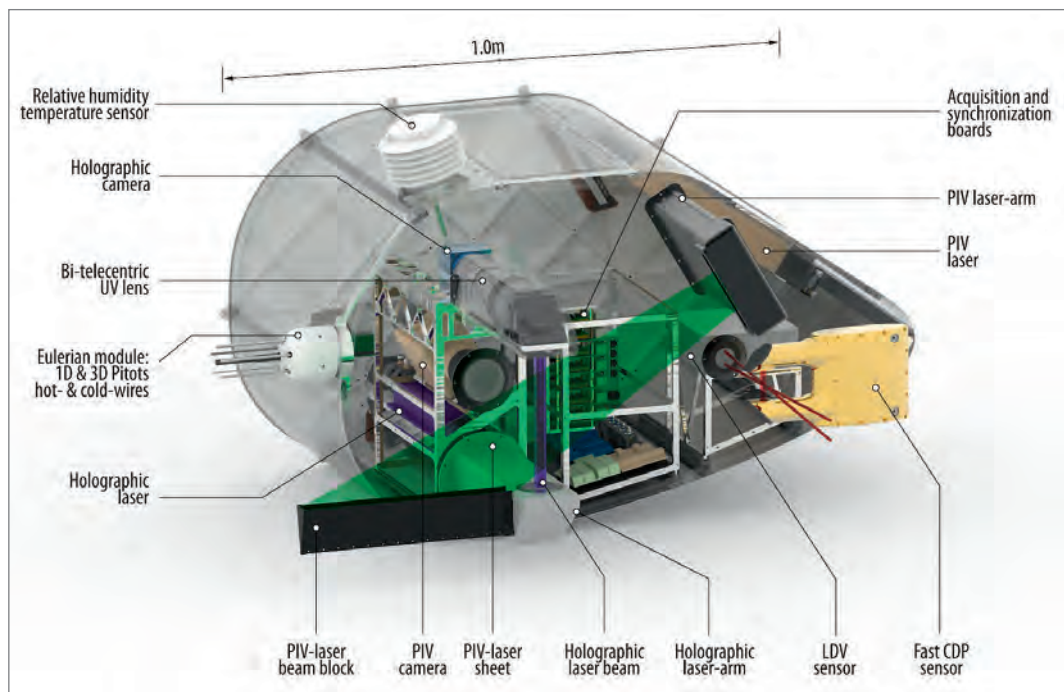

Fig. 5: CAD visualisation of the CloudKite instrument box, which can perform autonomous measurements in the air or on the deck of the UFS. The double-cavity Nd:YAG PIV laser illuminates cloud droplets within a thin laser sheet with double pulses at short time intervals. A high-speed digital camera captures image pairs of the illuminated droplets that can be used for PIV or PTV analysis.
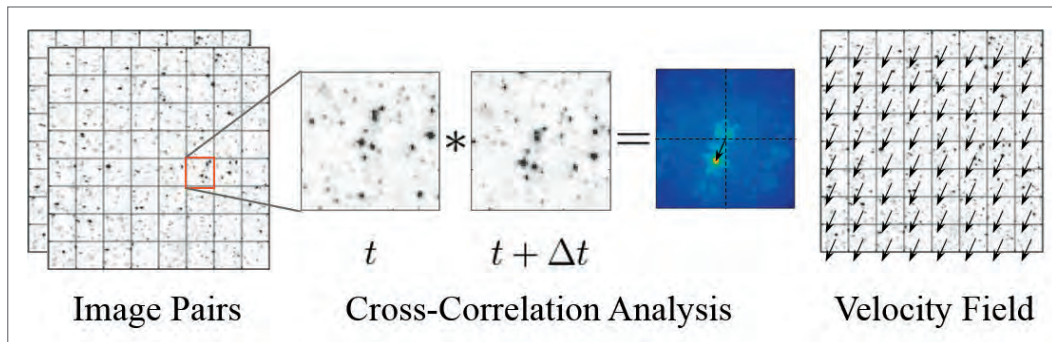
Fig. 6: Working principle of 2D PIV analysis: (a) start with image pairs divided into interrogation windows, (b) calculation of displacement, and (c) determination of velocity field.

Figure 6 illustrates the operating principle of 2D PIV. Before measurement, a calibration is performed to map camera images to a 2D plane coincident with the laser sheet. Pattern-matching between image pairs measures the displacement field Δx of particles in the plane. Since the particles follow the flow, the velocity field v is estimated as $v = \Delta x/\Delta t$. Image pairs are analysed piece-wise by subdividing them into Interrogation Windows or IWs (A). The spatial cross-correlation function is computed between IWs of image pairs (B). This correlation function has a maximum or "peak" at a location, which corresponds to the displacement Δx of the particle pattern and can be located to sub-pixel accuracy. Performing this procedure for all IWs yields 2D vector fields (C). Modern PIV algorithms iterate this procedure over multiple passes in a predictor-corrector scheme to enhance accuracy and dynamic range and incorporate additional steps to filter the result and reject obvious measurement errors. Several (tens of) open source and commercial software packages are available to perform this process.

Three basic rules of thumb inform the design of PIV measurements (Raffel 2007). Firstly, the seeding concentration should be sufficiently high to ensure around ten particles or more can be matched between IWs. Secondly, the maximum displacement should not exceed around one-quarter of the interrogation window size. Thirdly, the maximum displacement difference across each IW is limited to a fraction (3 % or so) of the IW size. Violation of any of these criteria by even a factor of two substantially reduces the measurement reliability. Coupled with limits on displacement measurement accuracy, these constraints limit the measurement accuracy of PIV to about 1 % of full range at best. For a given flow and spatial resolution, measurement accuracy is optimised by selecting the largest feasible Δt. In field measurements, the flow velocity and turbulence intensity can significantly vary over a timescale of seconds. The CloudKite incorporates a system to select an optimal Δt in real-time for each snapshot of the flow taken. This is accomplished using a pitot tube to estimate the bulk flow velocity at the time of the measurement, from which Δt is set.

22.3.2 Lagrangian Particle Tracking

Like PIV, Lagrangian Particle Tracking is an optical velocimetry technique capable of making two- or three-dimensional velocity and acceleration measurements of particles from recorded images of their motion. It can be combined with photogrammetric or holographic techniques to measure particle size. Extensive developments have been made over its five-decade history, summarised by (Dracos 1996) and (Raffel2018). Owing to the simplicity of the technique, several groups within the fluid mechanics community have developed LPT codes, many of which are publicly available.

In contrast to PIV, which examines groups of particles, LPT involves the optical tracking of individual particles. Because of the requirement to unambiguously identify and follow particles, LPT is typically limited to simultaneously measuring an order of magnitude fewer particles than a comparable PIV measurement. This significantly reduces the spatial information simultaneously available. On the other hand, since flow information is localised to the position of individual particles rather than averaged over an interrogation window, very high spatial resolution can be achieved. The most significant benefit of LPT is the ability to examine the flow evolution from a Lagrangian perspective, moving with the flow. This makes it a natural tool for the study of turbulent transport and mixing (Yeung 2002) and droplet formation in clouds (Shaw 2003), which are problems most conveniently analysed in the Lagrangian frame.
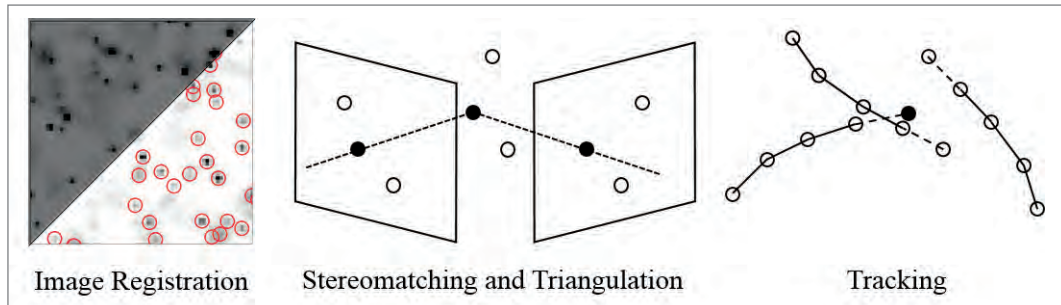
22

Fig. 7: The core steps of 3D Lagrangian Particle Tracking

Several variations on particle tracking methods exist (Maas et al. 1993; Dracos 1996; Ouellette et al. 2006; Schanz et al. 2016). Most operate on time-resolved videos of particle motion, captured from multiple perspectives. Although implementations differ, the core steps are illustrated in Figure 7. These are: image registration, where particle images are identified and their positions located on the image plane; stereo-matching and triangulation, where correspondences are made between particle images across cameras to reconstruct 3D particle positions; and tracking, where particles in one frame are associated with their trajectories through previous frames. This process is performed sequentially, building up tracks by stepping through each video frame. Particle velocity and acceleration are obtained by numerically differentiating its position measurement.

One exciting application of LPT at UFS is to explore the formation and collision of cloud droplets in situ. Figure 8 shows the setup of the Seesaw experiment at UFS, which implements a 3D LPT setup. Three cameras are mounted on a vibration damped camera box on a moving sled, sat amongst the clouds on the rooftop of UFS. Light from a fibre-coupled, pulsed laser is used to provide volumetric illumination of a common field-of-view shared between cameras. This allows us to simultaneously record videos of ambient water droplets from three perspectives.

The Seesaw experiment at UFS has a number of unique features optimised for cloud measurements (Bertens et al. 2021). The most striking feature is the sled, which allows the cameras to follow particles as they are swept along by the prevailing wind. By doing so, the residence time of the particles within the measurement volume is extended to sample each particle hundreds of times on its passage through the volume. This is necessary to reliably measure each particle's motion and properties. Considerable technical effort has been expended in the design of the 3D LPT setup to minimise its weight, whilst maintaining enough stiffness to accelerate up to 5 m/s and stop again over a distance of only 5 m. Stringent requirements upon the temporal resolution, which oversamples the Kolmogorov timescale by a factor of 100, have been achieved. These are necessary to reliably measure the Lagrangian acceleration (Mordant et al. 2004), which exhibits rapid, extreme fluctuations hundreds of standard deviations in excess of the mean. Additional effort has been made in the automation of data acquisition systems, which can support
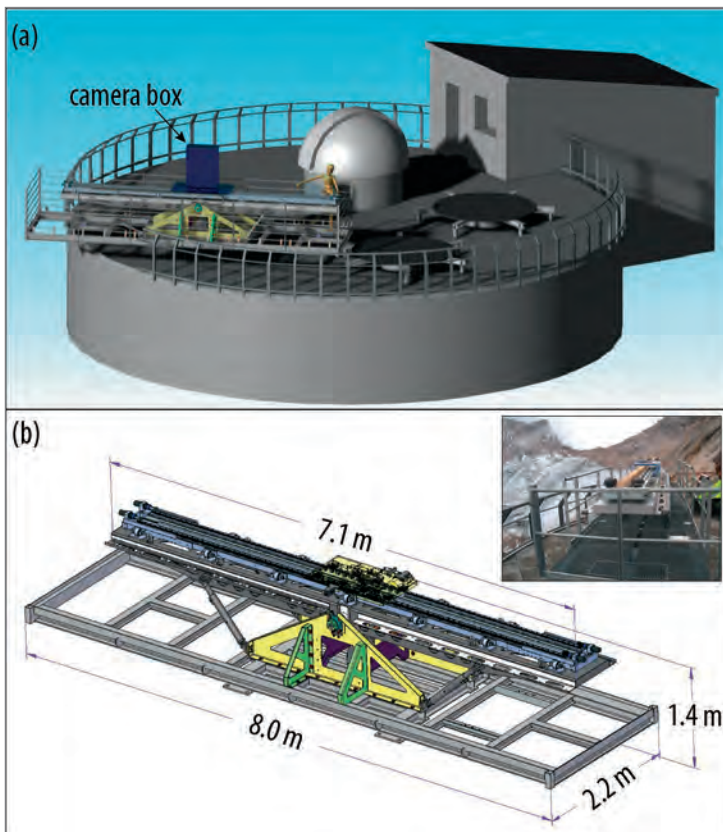

Fig. 8: Schematic (a) of Seesaw LPT experiment situated on the rooftop of UFS and (b) a detailed view of the camera box. Using angled mirrors, the three cameras are able to view droplets as they are illuminated by a laser beam from above.

a peak data acquisition rate of 4 TB of images per hour thanks to the direct integration of the experiment with a high performance computing and storage cluster. The high data throughput is necessary to acquire a statistically converged sampling of transient clouds, which have a typical duration of tens of minutes.

The experimental challenges of working in the field impact the particle tracking algorithms used to process the data. Despite moving with the flow, a large measurement volume is required to ensure sufficiently long residence times due to the unpredictability of the droplet's velocity. This results in a low illuminating power density, requiring the use of large apertures and shallow viewing angles and results in the majority of droplets' images being out-of-focus on the sensor. Extracting accurate position information under these circumstances requires state-of-the-art techniques, which we have developed building upon the Shake The Box algorithm (Schanz 2016). The approach is to improve the efficiency of the image registration and tracking steps (see Figure 7) by accurately modelling the images formed by droplets upon the camera sensor over an entire video sequence. By fitting this model to the observed images, the reliability and accuracy of image registration is improved enough to track over 10'000 droplets simultaneously.

22.4 Optical measurement of particle size and shape

Phase Doppler Interferometry (PDI), also known as Phase Doppler Particle Analyzer (PDPA), is a technique to measure one velocity component, size, and sometimes phase (Bachalo 1980; Chuang et al. 2008). A dual PDI probe in a cloud on the UFS and a diagram of its operation are shown in Figure 9. One laser beam is split into two equal beams which are crossed in a small volume with an angle 2α between them. The split beams $\vec{E}_\pm = \frac{1}{2}\vec{E}_0 \exp\left[i(kx\cos\alpha \pm ky\sin\alpha - \omega t)\right]$ interfere producing $\vec{E}_+ + \vec{E}_- = \vec{E}_0 \cos(ky\sin\alpha)\exp\left[i(kx\cos\alpha - \omega t)\right]$, which is a series of x-oriented interference fringes.

A particle in the overlap acts as a lens and mirror for the fringes. One or more photodetectors record the reflected or refracted fringes, which sweep past the detector/s as the particle moves in the y-direction. The detectors record so called Doppler bursts of the sweeping fringes. For approximately spherical particles (water and some ice), the Doppler burst frequency is related to velocity by $f_d = \frac{1}{\pi}k|v_y|\sin\alpha$, while the difference in phase between photodetectors is related to size (Bachalo 1980; Chuang et al. 2008). The special case of only one detector is Laser Doppler Velocimetry/Anemometry (LDV/A, see Foreman et al., 1965), which cannot obtain size.

In practice, however, three or more detectors are used to to resolve particle diameter over a large range by resolving phase ambiguity and a small frequency shift is applied to one split beam to make sweeping fringes so that the sign of v_y can be determined and $v_y \approx 0$ can be resolved reliably. See Bachalo (1980), Sankar et al. (1991) and Chuang et al. (2008) for more details.
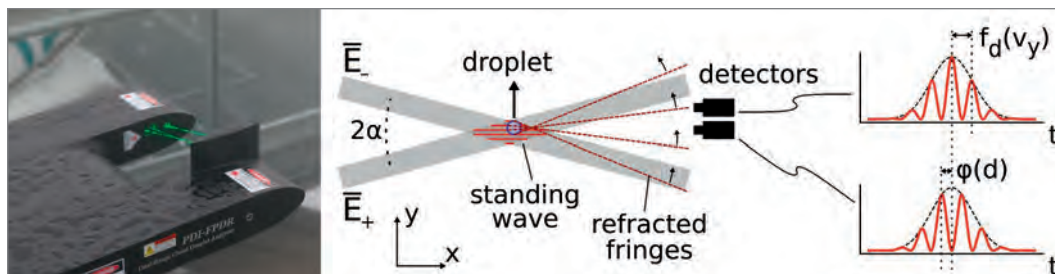

Fig. 9: (left) Dual PDI probe in a cloud at the UFS. (right) The working principle of Phase Doppler Interferometry (PDI). A laser beam is split and made to overlap producing fringes. A droplet passes through, causing refracted fringes to sweep, which are recorded as Doppler bursts by photodetectors. The frequency and phase differences between the Doppler bursts are related to the droplet y-velocity and diameter.
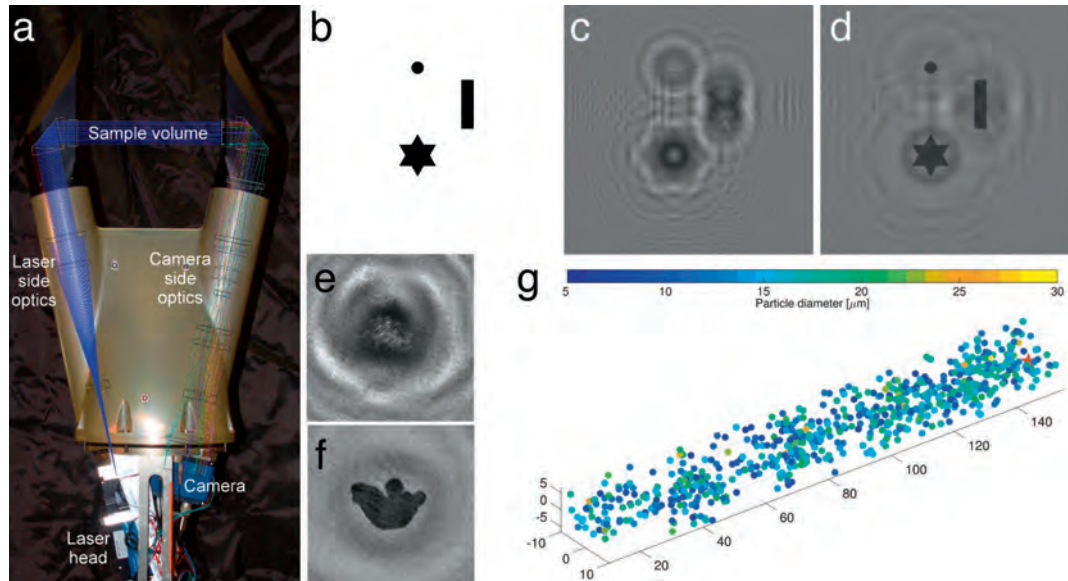
Fig. 10: (a) The HALOHolo instrument (Schlenczek 2018). (b) Mask of three obstructions used for the synthetic hologram in (c) which are a 100 μm circle, a 100 μm × 400 μm rectangle, and a 300 μm wide sixpointed star. (c) Synthetic hologram for (b) 10 cm away from the mask for 355 nm light. (d) Reconstruction of (c) using the technique of Fugal et al. (2009). (e) Measured hologram of an ice particle. (f) Reconstruction of (e) using the technique of Fugal et al. (2009). (g) Positions (mm) and sizes of cloud droplets (color-coded) measured by 4 HALOHolo at UFS on 25 September 2019, 10:29:59 UTC. The position of the ice particle from (e) and (f) is shown as a red star.

Another interference technique is holography, which can measure many particle positions, sizes, and shapes simultaneously. The most common setup is in-line holography where a coherent light beam is sent through the volume and the diffraction pattern resulting from the beam and the light occluded and scattered by the particles is captured by a camera (Borrmann & Jaenicke 1993; Henneberger et al. 2013; Spuler & Fugal 2011). An example instrument, HALOHolo, is shown in Fig. 10a. The diffraction patterns cast by an obstruction in the beam (e.g. a particle) are a function of the distance from the obstruction to the camera, its size, and its shape. Fig. 10b shows a circle, a rectangle, and a six-pointed star obstructions. Their calculated diffraction patterns are shown in Fig. 10c. The interference patterns acquired by the camera must be reconstructed, which consists of diffracting the acquired image backwards (such as in Fig. 10d), to get the particle shapes, sizes, and positions which includes the distance from the camera. A hologram and its reconstruction from a measured ice particle are shown in Fig. 10e and 10f. The particle positions and sizes from a hologram obtained on 25 September 2019 from a long-lasting cloud at the UFS are shown in Fig. 10 g.

The main advantages of holography are that it can be done with one camera and few optical elements, a weak laser, and a large depth of field. However, hologram reconstruction is very expensive in person hours (analog) or computation time (digital) (Schlenczek 2018). Depth resolution is limited, although a dual inline holography setup can mitigate this at the cost of added complexity and great difficulty in field use (Raupach et al. 2006). It is also difficult to distinguish the phase between small droplets and approximately spherical ice particles (Korolev et al. 2017). Notable results from holography in clouds include the observation of nonuniform droplet spatial distributions (Borrmann et al. 1993; Uhlig et al. 1998), partitioning of ice and droplets in mixed-phase clouds (Lohmann et al. 2016; Schlenczek 2018), size and spatial distributions in ice clouds (O'Shea et al. 2016; Schlenczek et al. 2017), and the analysis of mixing in convective clouds (Beals et al. 2015).

22.5 Outlook

With the Seesaw experiment at UFS, it will become possible for the first time to study the effect of gravity on the acceleration and velocity statistics of the drops in a high-Reynolds number turbulent flow with small ε. Since the accelerations and velocities involved are rather small, the shaking of the 3D LPT setup must be kept to a minimum in order not to introduce an artificial signal to the data. This is possible by carefully selecting the acceleration profile of the sled for each given velocity, isolating the vibrations of the sled from the setup via dampers and springs, and finally measuring and subtracting any remaining vibrations using a set of accelerometers.

We are also working on a way to use the existing LPT setup to measure the size of each individual droplet within our measurement volume, based on the amount of light it scatters onto the sensor. Given that we have data from 3 cameras available, each at a slightly different angle with respect to the incident laser beam, and that we track each droplet over substantial length of time, it should be possible to deduce the droplet size by reference to the known Mie scattering curves. This would allow conditioning droplet statistics on their size and yield more insight into the dynamics, as opposed to kinematics, of these objects.

We plan on eventually flying the Cloudkite (instrument diagram in Figure 5) from the Zugspitze to perform PIV (or 2-frame LPT when the particle concentration is low), holographic, hotwire, etc. measurements in clouds further from the mountainside (about 500 m) to reduce topographic effects. The Cloudkite will have a very high volumetric sample rate (~1 L/s) in order to get large statistics on the positions and sizes of cloud particles seen by its holography system, and cloud and particle velocities from its PIV system.

Combining the seesaw, the ultrasonic anemometers, and likely the HALOHolo instrument from Figure 10a on the deck of the UFS with the Cloudkite in the sky above; we hope to look at cloud microphysics at unprecedented detail including performing two point measurements from the ground and the Cloudkite at the same time which is important for looking at the spatial variation of particle dynamics within clouds. We hope these measurements will better elucidate the 'cloud problem'. Eventually, we hope that the subgrid cloud modelling of clouds in weather and climate models will be improved so that we can better predict the weather and climate.

References

Adrian, R. J., 1991. Particle-Imaging Techniques for Experimental Fluid Mechanics. *Annual Review of Fluid Mechanics*, 23(1), pp. 261–304. Available at: http://www.annualreviews.org/doi/abs/10.1146/annurev.fl.23.010191.001401.

Adrian, R. J., 2005. Twenty years of particle image velocimetry. *Experiments in Fluids*, 39(2), pp.159–169.

Adrian, R. J. & Westerweel, J., 2011. *Particle Image Velocimetry*,

Bachalo, W. D., 1980. Method for measuring the size and velocity of spheres by dual-beam light-scatter interferometry. *Applied Optics*, 19(3), p.363. Available at: https://www.osapublishing.org/abstract.cfm?URI=ao-19-3-363.

Balachandar, S. & Eaton, J. K., 2010. Turbulent Dispersed Multiphase Flow. *Annual Review of Fluid Mechanics*, 42(1), pp.111–133. Available at: http://www.annualreviews.org/doi/10.1146/annurev.fluid.010908.165243.

Beals, M. J. et al., 2015. Holographic measurements of inhomogeneous cloud mixing at the centimeter scale. *Science*, 350(6256), pp.87–90. Available at: http://www.sciencemag.org/cgi/doi/10.1126/science.aab0751.

Bec, J. et al., 2007. Heavy Particle Concentration in Turbulence at Dissipative and Inertial Scales. *Physical Review Letters*, 98(8), p.84502. Available at: https://link.aps.org/doi/10.1103/PhysRevLett.98.084502.

Bertens, G., Bagheri, G., Xu, H., Bodenschatz, E. & Moláček, J., 2021. In situ particle tracking experiment. Review of Scientific Instruments, 92,p 125105

Bodenschatz, E. et al., 2010. Can we understand clouds without turbulence? *Science*, 327(5968), pp. 970–971.

Bodenschatz, E., 2015. Clouds resolved. *Science*, 350(6256), pp.40–41. Available at: http://www.sciencemag.org/cgi/doi/10.1126/science.aad1386.

Bodenschatz, E. et al., 2014. Variable density turbulence tunnel facility. *Review of Scientific Instruments*, 85(9), p.93908. Available at: http://scitation.aip.org/content/aip/journal/rsi/85/9/10.1063/1.4896138.

22

Borrmann, S. & Jaenicke, R., 1993. Application Of Microholography for Ground-based In Situ Measurements in Stratus Cloud Layers: A Case Study. *Journal of Atmospheric and Oceanic Technology*, 10(3), pp. 277–293. Available at: http://journals.ametsoc.org/doi/abs/10.1175/1520-0426%281993%29010%3C0277%3AAOMFGB%3E2.0.CO%3B2.

Borrmann, S., Jaenicke, R. & Neumann, P., 1993. On spatial distributions and inter-droplet distances measured in stratus clouds with in-line holography. *Atmospheric Research*, 29(3–4), pp. 229–245. Available at: http://linkinghub.elsevier.com/retrieve/pii/0169809593900059.

Celani, A., 2007. The frontiers of computing in turbulence: challenges and perspectives. *Journal of Turbulence*, 8 (October 2014), p. N34. Available at: https://www.tandfonline.com/doi/full/10.1080/14685240601091668.

Chuang, P.Y. et al., 2008. Airborne Phase Doppler Interferometry for Cloud Microphysical Measurements. *Aerosol Science and Technology*, 42(8), pp. 685–703. Available at: http://www.tandfonline.com/doi/abs/10.1080/02786820802232956.

Darcy, H., 1858. Note relative à quelques modifications à introduire dans le tube de Pitot. In *Annales des Ponts et Chaussées*. pp. 351–359.

Davidson, P., 2015. *Turbulence: an introduction for scientists and engineers*, Oxford University Press, USA.

DIN EN 60751 / IEC 60751, 2008. *Industrial platinum resistance thermometers and platinum temperature sensors.*

Dracos, T., 1996. *Particle tracking in three-dimensional space*, Dordrecht: Kluwer.

Falkovich, G., Fouxon, A. & Stepanov, M.G., 2002. Acceleration of rain initiation by cloud turbulence. *Nature*, 419(6903), pp.151–154.

Fan, Y. et al., 2015. Nanoscale sensing devices for turbulence measurements. *Experiments in Fluids*, 56(7), p.138. Available at: http://link.springer.com/10.1007/s00348-015-2000-0.

Foreman, J.W., George, E.W. & Lewis, R.D., 1965. MEASUREMENT OF LOCALIZED FLOW VELOCITIES IN GASES WITH A LASER DOPPLER FLOWMETER. *Applied Physics Letters*, 7(4), pp.77–78. Available at: http://dx.doi.org/10.1063/1.1754319.

Fugal, J.P., Schulz, T.J. & Shaw, R.A., 2009. Practical methods for automated reconstruction and characterization of particles in digital in-line holograms. *Measurement Science and Technology*, 20(7), p. 75501. Available at: http://stacks.iop.org/0957-0233/20/i=7/a=075501?key=crossref.fa5f591f6ae0efdc367574230506c8b8.

Grabowski, W.W. & Wang, L.-P., 2013. Growth of Cloud Droplets in a Turbulent Environment. *Annual Review of Fluid Mechanics*, 45(1), pp. 293–324. Available at: http://www.annualreviews.org/doi/abs/10.1146/annurev-fluid-011212-140750.

Gunn, R. & Kinzer, G.D., 1949. THE TERMINAL VELOCITY OF FALL FOR WATER DROPLETS IN STAGNANT AIR. *Journal of Meteorology*, 6(4), pp.243–248. Available at: http://journals.ametsoc.org/doi/abs/10.1175/1520-0469%281949%29006%3C0243%3ATTVOFF%3E2.0.CO%3B2.

Harrison, G., 2014. *Meteorological measurements and instrumentation*, Chichester, UK: Wiley Blackwell.

Henneberger, J. et al., 2013. HOLIMO II: a digital holographic instrument for ground-based in situ observations of microphysical properties of mixed-phase clouds. *Atmospheric Measurement Techniques*, 6(11), pp.2975–2987. Available at: http://www.atmos-meas-tech.net/6/2975/2013/.

Ishihara, T. et al., 2016. Energy spectrum in high-resolution direct numerical simulations of turbulence. *Physical Review Fluids*, 1(8), p.82403. Available at: https://link.aps.org/doi/10.1103/PhysRevFluids.1.082403.

Jameson, A.R. & Kostinski, A.B., 2001. What is a Raindrop Size Distribution? *Bulletin of the American Meteorological Society*, 82(6), pp.1169–1177. Available at: http://journals.ametsoc.org/doi/abs/10.1175/1520-0477(2001)082%3C1169:WIARSD%3E2.3.CO;2.

Jimenez, J., 2003. Computing high-Reynolds-number turbulence: will simulations ever replace experiments? *Journal of Turbulence*, 4(September 2002), pp.16–18. Available at: http://www.informaworld.com/openurl?genre=article&doi=10.1088/1468-5248/4/1/022&magic=crossref%7C%7CD404A21C5BB-053405B1A640AFFD44AE3.

King, L.V., 1914. On the Convection of Heat from Small Cylinders in a Stream of Fluid: Determination of the Convection Constants of Small Platinum Wires, with Applications to Hot-Wire Anemometry. *Proceedings of the Royal Society A: Mathematical, Physical and Engineering Sciences*, 90(622), pp.563–570. Available at: http://rspa.royalsocietypublishing.org/cgi/doi/10.1098/rspa.1914.0089.

Kolmogorov, A.N., 1941. The local structure of turbulence in incompressible viscous fluid for very large Reynolds numbers. In *Dokl. Akad. Nauk SSSR*. pp. 299–303.

Korolev, A. et al., 2017. Mixed-Phase Clouds: Progress and Challenges. *Meteorological Monographs*, 58 (Fahrenheit 1724), p.5.1–5.50. Available at: http://journals.ametsoc.org/doi/10.1175/AMSMONO-GRAPHS-D-17-0001.1.

Kostinski, A.B. & Shaw, R.A., 2005. Fluctuations and Luck in Droplet Growth by Coalescence. *Bulletin of the American Meteorological Society*, 86(2), pp. 235–244. Available at: http://journals.ametsoc.org/doi/abs/10.1175/BAMS-86-2-Kostinski.

Langmuir, I., 1948. THE PRODUCTION OF RAIN BY A CHAIN REACTION IN CUMULUS CLOUDS AT TEMPERATURES ABOVE FREEZING. *Journal of Meteorology*, 5(5), pp.175–192. Available at: http://journals.ametsoc.org/doi/abs/10.1175/1520-0469%281948%29005%3C0175%3ATPORBA%3E2.0.CO%3B2.

Levich, V. G., 1954. The Theory of Coagulation of Colloids in Turbulent Liquid Stream. In *Dokl. Akad. Nauk SSSR*. pp. 809–812.

Lohmann, U. et al., 2016. Persistence of orographic mixed-phase clouds. *Geophysical Research Letters*, 43(19), p.10,512–10,519. Available at: http://doi.wiley.com/10.1002/2016GL071036.

Maas, H. G., Gruen, A. & Papantoniou, D., 1993. Particle tracking velocimetry in three-dimensional flows. *Experiments in Fluids*, 15(2), pp.133–146. Available at: http://link.springer.com/10.1007/BF00190953.

Malinowski, S. P. et al., 2013. Physics of Stratocumulus Top (POST): turbulent mixing across capping inversion. *Atmospheric Chemistry and Physics*, 13(24), pp.12171–12186.

Marshall, J. S. & Palmer, W. M. K., 1948. THE DISTRIBUTION OF RAINDROPS WITH SIZE. *Journal of Meteorology*, 5(4), pp.165–166. Available at: http://doi.wiley.com/10.1002/qj.49707632704.

McKeon, B. et al., 2007. Velocity, vorticity, and Mach number. In *Springer Handbook of Experimental Fluid Mechanics*. Springer, pp. 215–471.

Mordant, N., Crawford, A. M.M. & Bodenschatz, E., 2004. Experimental Lagrangian acceleration probability density function measurement. *Phys. D Nonlinear Phenom.*, 193(1–4), pp. 245–251. Available at: http://linkinghub.elsevier.com/retrieve/pii/S0167278904000417.

O'Shea, S. J. et al., 2016. Airborne observations of the microphysical structure of two contrasting cirrus clouds. *Journal of Geophysical Research: Atmospheres*, 121(22), p.13,510–13,536. Available at: http://doi.wiley.com/10.1002/2016JD025278.

Ouellette, N.T., Xu, H. & Bodenschatz, E., 2006. A quantitative study of three-dimensional Lagrangian particle tracking algorithms. *Exp. Fluids*, 40(2), pp.301–313. Available at: http://link.springer.com/10.1007/s00348-005-0068-7.

Pitot, H. de, 1732. Description d'une machine pour mesurer la vitesse des eaux courantes et le sillage des vaisseaux. *Mémoires de L'Académie*.

Pope, S. B., 2000. *Turbulent flows*, Cambridge university press.

La Porta, A. et al., 2001. Fluid particle accelerations in fully developed turbulence. *Nature*, 409(6823), pp.1017–1019. Available at: http://www.nature.com/doifinder/10.1038/35059027.

Pumir, A. & Wilkinson, M., 2016. Collisional Aggregation Due to Turbulence. *Annual Review of Condensed Matter Physics*, 7(1), pp.141–170. Available at: http://arxiv.org/abs/1508.01538.

Raffel, M., 2007. *Particle image velocimetry a practical guide*, Heidelberg New York: Springer.

Raupach, S. M.F. et al., 2006. Digital crossed-beam holography for in situ imaging of atmospheric ice particles. *J. Opt. A-Pure Appl. Op.*, 8(9), pp.796–806.

Richardson, L. F., 1922. *Weather prediction by numerical process*, Cambridge University Press.

Risius, S., 2012. *nvestigation of turbulent flows at the Umweltforschungsstation Schneefernerhaus (Zugspitze)*. Institute for Nonlinear Dynamics, Emden.

Risius, S. et al., 2015. Schneefernerhaus as a mountain research station for clouds and turbulence. *Atmospheric Measurement Techniques*, 8(8), pp. 3209–3218. Available at: http://www.atmos-meas-tech-discuss.net/8/541/2015/.

Saffman, P. G. & Turner, J. S., 1956. On the collision of drops in turbulent clouds. *Journal of Fluid Mechanics*, 1(1), p.16. Available at: http://www.journals.cambridge.org/abstract_S0022112056000020.

Sankar, S. V. et al., 1991. Sizing fine particles with the phase Doppler interferometric technique. *Applied Optics*, 30(33), p.4914. Available at: https://www.osapublishing.org/abstract.cfm?URI=ao-30-33-4914.

Scarano, F., 2013. Tomographic PIV: principles and practice. *Measurement Science and Technology*, 24(1), p.12001. Available at: http://stacks.iop.org/0957-0233/24/i=1/a=012001?key=crossref.06bb53d64ea-6b5ebccdce8da58d8006e.

Schanz, D., Gesemann, S. & Schröder, A., 2016. Shake-The-Box: Lagrangian particle tracking at high particle image densities. *Experiments in Fluids*, 57(5), p.70. Available at: http://link.springer.com/10.1007/s00348-016-2157-1.

Schlenczek, O., 2018. *Airborne and ground-based holographic measurement of hydrometeors in liquid-phase, mixed-phase and ice clouds*. University of Mainz.

Schlenczek, O. et al., 2017. Microphysical Properties of Ice Crystal Precipitation and Surface-Generated Ice Crystals in a High Alpine Environment in Switzerland. *Journal of Applied Meteorology and Climatology*, 56(2), pp.433–453. Available at: http://journals.ametsoc.org/doi/10.1175/JAMC-D-16-0060.1.

Shaw, R. a, 2003. Particle Turbulence Interactions in Atmospheric Clouds. *Annual Review of Fluid Mechanics*, 35(1), pp. 183–227. Available at: http://www.annualreviews.org/doi/abs/10.1146/annurev.fluid.35.101101.161125.

Siebert, H. et al., 2015. High-resolution measurement of cloud microphysics and turbulence at a mountain-top station. *Atmospheric Measurement Techniques*, 8(8), pp.3219–3228. Available at: http://www.atmos-meas-tech-discuss.net/8/569/2015/.

Siebert, H., Lehmann, K., Wendisch, M., et al., 2006. Probing Finescale Dynamics and Microphysics of Clouds with Helicopter-Borne Measurements. *Bulletin of the American Meteorological Society*, 87(12), pp.1727–1738. Available at: http://journals.ametsoc.org/doi/abs/10.1175/BAMS-87-12-1727.

Siebert, H. et al., 2010. Towards understanding the role of turbulence on droplets in clouds: in situ and laboratory measurements. *Atmospheric Research*, 97(4), pp.426–437.

22

Siebert, H., Lehmann, K. & Wendisch, M., 2006. Observations of Small-Scale Turbulence and Energy Dissipation Rates in the Cloudy Boundary Layer. *Journal of the Atmospheric Sciences*, 63(5), pp.1451–1466. Available at: http://journals.ametsoc.org/doi/abs/10.1175/JAS3687.1.

Siebert, H., Shaw, R. a. & Warhaft, Z., 2010. Statistics of Small-Scale Velocity Fluctuations and Internal Intermittency in Marine Stratocumulus Clouds. *Journal of the Atmospheric Sciences*, 67(1), pp.262–273. Available at: http://journals.ametsoc.org/doi/abs/10.1175/2009JAS3200.1.

Snyder, W. H. & Lumley, J. L., 1971. Some measurements of particle velocity autocorrelation functions in a turbulent flow. *Journal of Fluid Mechanics*, 48(1), pp. 41–71.

Spuler, S. M. & Fugal, J., 2011. Design of an in-line, digital holographic imaging system for airborne measurement of clouds. *Applied Optics*, 50(10), p.1405. Available at: https://www.osapublishing.org/abstract.cfm?URI=ao-50-10-1405.

Stevens, B. & Bony, S., 2013. What Are Climate Models Missing? *Science*, 340(6136), pp.1053–1054. Available at: http://www.ncbi.nlm.nih.gov/pubmed/23723223.

Taylor, G. I., 1938. The Spectrum of Turbulence. *Procdings of the Royal Society A: Mathematical, Physical and Engineering Sciences*, 164(919), pp. 476–490. Available at: http://www.jstor.org/stable/97077.

Uhlig, E.-M., Borrmann, S. & Jaenicke, R., 1998. Holographic in-situ measurements of the spatial droplet distribution in stratiform clouds. *Tellus B*, 50(4), pp. 377–387. Available at: http://www.tellusb.net/index.php/tellusb/article/view/16210.

Vaillancourt, P.A. & Yau, M.K., 2000. Review of Particle – Turbulence Interactions and Consequences for Cloud Physics. *Bulletin of the American Meteorological Society*, 81(2), pp. 285–298. Available at: http://journals.ametsoc.org/doi/abs/10.1175/1520-0477%282000%29081%3C0285%3AROPIAC%3E2.3.CO%3B2.

Voth, G.A., Satyanarayan, K. & Bodenschatz, E., 1998. Lagrangian acceleration measurements at large Reynolds numbers. *Phys. Fluids*, 10(9), pp. 2268–2280. Available at: http://aip.scitation.org/doi/10.1063/1.869748.

Wallace, J. M. & Hobbs, P. V., 2006. Cloud Microphysics. In *Atmospheric Science*. Elsevier, pp. 209–269. Available at: http://linkinghub.elsevier.com/retrieve/pii/B9780127329512500119.

Warhaft, Z., 2002. Turbulence in nature and in the laboratory. *Proceedings of the National Academy of Sciences of the United States of America*, 99 Suppl 1, pp. 2481–2486.

Westerweel, J., Elsinga, G. E. & Adrian, R. J., 2013. Particle Image Velocimetry for Complex and Turbulent Flows. *Annual Review of Fluid Mechanics*, 45(1), pp. 409–436. Available at: http://www.annualreviews.org/doi/10.1146/annurev-fluid-120710-101204.

Yeung, P. K., 2002. LAGRANGIAN INVESTIGATIONS OF TURBULENCE. *Annual Review of Fluid Mechanics*, 34(1), pp.115–142. Available at: http://www.annualreviews.org/doi/10.1146/annurev.fluid.34.082101.170725.

Yeung, P.K., Zhai, X.M. & Sreenivasan, K.R., 2015. Extreme events in computational turbulence. *Proceedings of the National Academy of Sciences*, 112(41), pp.12633–12638. Available at: http://www.pnas.org/lookup/doi/10.1073/pnas.1517368112.

Yoshimoto, H. & Goto, S., 2007. Self-similar clustering of inertial particles in homogeneous turbulence. *Journal of Fluid Mechanics*, 577, p.275. Available at: http://www.journals.cambridge.org/abstract_S0022112007004946.